Flow structure in a model of aircraft trailing vortices

J. M. Faddy and D. I. Pullin
Graduate Aeronautical Laboratories 105-50, California Institute of Technology, Pasadena, California 91125

(Received 8 December 2004; accepted 27 May 2005; published online 23 August 2005)

We consider a model of incompressible trailing vortices consisting of an array of counter-rotating structures in a doubly periodic domain, infinite in the vertical direction. The two-dimensional vortex array of Mallier and Maslowe is combined with an axial velocity profile chosen proportional to the initial axial vorticity to provide an initial condition for the vortex wake. This base flow is a weak solution of the steady Euler equations with three velocity components that are functions of two spatial coordinates, thus allowing its linear stability properties to be investigated. These are used to interpret several stages in the development of vortex structure observed in fully three-dimensional direct numerical simulation (DNS) at Reynolds numbers $\Gamma/(2\pi\nu)=\mathcal{O}(1000)$. For sufficiently high axial velocity, its effect can be seen, in that each vortex in the linear array first develops helical structures before undergoing a period of relaminarization. At later times the more slowly growing cooperative elliptical instabilities become apparent, but the helical structure persists and the observed vortical structures remain coherent for longer periods than in the absence of axial velocity. Using the stretched-vortex subgrid model, large-eddy simulation runs are performed at large Reynolds numbers and a mixing transition identified at about $\mathrm{Re}=1-2\times10^4$. Similar phenomena are observed in these simulations as are seen in the DNS. © *2005 American Institute of Physics*. [DOI: 10.1063/1.1955536]

I. INTRODUCTION

The wake shed by lifting bodies such as an aircraft wing rolls up and forms a pair of counter-rotating vortices that can persist back to the original location of the airfoil start-up process.[1] In practice, viscous and turbulent diffusion as well as atmospheric turbulence and vortex-related instabilities result in decaying the strength of wing-tip vortices; however, they have been observed to persist tens of miles downstream of large aircraft.[2] These vortices pose a significant risk to following aircraft, particularly during take off and landing where insufficient time may have passed for their decay.[2] An understanding of the underlying physical processes within a turbulent vortex is therefore of pressing practical importance. Studies of coherent structures have shown that many turbulent flows comprise such thin organized vortical structures of various sizes intertwined with each other. These observations, coupled with a knowledge of the dynamics of vortical structures and the instabilities arising from their interaction, can aid in developing understanding and simplified models of the full turbulent flow field. In this paper, we consider an array of counter-rotating structures as a model for the trailing vortex wake, and use the linear stability properties of the base flow to aid in the interpretation of its nonlinear evolution.

An elementary abstraction of a vortical flow is the axisymmetric Rankine vortex comprising a circular core of uniform vorticity surrounded by an irrotational flow. Kelvin[3] studied the stability of this flow and showed it to be marginally stable with respect to sinusoidal displacement disturbances; these bending waves simply rotate around the vortex. If the azimuthal component of an imposed external strain field balances this self-induced rotation, disturbances will grow exponentially due to the radial component of the strain field. It has been shown[4] that when this strain is generated by a counter-rotating vortex pair, there is instability of perturbations that are symmetric with respect to the plane separating the vortex. This is associated with the lowest Kelvin mode corresponding to a simple displacement of the entire vortex core. Widnall, Bliss, and Tsai[5] identified short-wavelength bending instabilities by considering a weakly strained Rankine vortex as a model of the vortex pair. The physical mechanism behind these instability modes is a resonant interaction between the strain and Kelvin waves with azimuthal wave numbers $m=\pm1$ at the same axial frequency. Waves with $|m|>1$ are axial waves that do not deflect the vortex axis. Instability modes occurring via an analogous resonant growth of $m=0$ and $m=\pm2$ have been identified.[6] All of these pair instabilities fall within a more general class of elliptic instabilities where two-dimensional flows with elliptic streamlines are unstable to three-dimensional disturbances.[7,8]

A more realistic vortex has a continuous distribution of vorticity with no clearly defined core. Hoffmann and Joubert[9] argued that a turbulent vortex is characterized by a central core region of solid-body rotation surrounded by a region in which the Reynolds stress dominates and the circulation varies logarithmically with radius. At larger radii, Govindaraju and Saffman[10] showed that if the vortex grows at a rate faster than that due to molecular diffusion alone, an overshoot in circulation must develop, followed by a long tail of small negative gradient. Utilizing an inviscid theory for the roll up of a vortex sheet, Moore and Saffman[11] analyzed the internal structure of a laminar trailing vortex, showing that axial velocity must be present, whose magnitude and direction depend upon the wing-tip loading. The

effect that jet- and wake-like axial velocity profiles have on the development of a turbulent line vortex was studied experimentally by Phillips and Graham.[12] They found that imposing an axisymmetric jet or a wake resulted in greater turbulence intensities and Reynolds shear stresses within the vortex, the former having the stronger effect.

The Lamb-Oseen vortex, defined by a vorticity distribution that decreases exponentially with the square of the radius, represents the flow field that results from a decaying line vortex and is often chosen as a physically realistic base flow for analyzing trailing vortices. In cylindrical coordinates, the Lamb-Oseen vortex is defined by an azimuthal velocity u_θ^* that varies with radius r^* as

$$u_\theta^*(r^*) = \frac{\Gamma^*}{2\pi r^*}\left(1 - e^{(r^*/\delta^*)^2}\right), \tag{1}$$

where Γ^* is the vortex circulation, δ^* is some length scale ($2\sqrt{\nu t}$ for the decaying line vortex) and the "*" superscript denotes dimensional quantities. A convenient Reynolds number is then defined as $\mathrm{Re}=\Gamma^*/2\pi\nu^*$. This flow is Rayleigh stable. A strain field produced by an axial velocity proportional to the vorticity is sufficient to render the flow linearly unstable[13] for small values of the swirl parameter q, defined in terms of the relative strength of the swirling velocity to the axial flow;

$$u_x^*(r) = u_d^* e^{-(r^*/\delta^*)^2}, \quad q = \frac{\Gamma^*}{2\pi\delta^* u_d^*}, \tag{2}$$

where u_d^* is the maximum axial velocity. The combination of (1) and (2) is called the Batchelor vortex. Direct numerical simulation (DNS) and large-eddy simulation (LES)[14–16] with initial conditions given by the Batchelor vortex have shown that, although the base flow is linearly unstable, nonlinear interactions drive the flow evolution toward a stable configuration through a weakening of the axial flow. As q increases dynamically, disturbances in the vortex core are damped and the core rotation ultimately results in a relaminarization. Such simulations typically employ the temporal approximation, which aims to represent the spatial evolution of the flow by the transient development of a finite-length segment of the domain. Imposing periodicity in the axial direction then results in a realizable simulation. In most implementations this eliminates, from the axial momentum equation, the influence of any mean pressure gradients that may develop in the vortex core, consequently preventing the distinction between a jet and a wake.

Presently, we consider a model for trailing vortices based on an initial condition comprising an array of counter-rotating vortices. In Sec. II we define the flow geometry and formulate the governing equations for analyzing this flow. An axial velocity that is modeled on vortex roll-up and chosen proportional to the initial axial vorticity is superimposed with a corresponding swirl parameter q chosen analogous to the Batchelor vortex. The current formulation has two attractive properties. First, it allows the straining effect of image vortices to be retained in a self-consistent manner. Second, the base flow is an exact solution of the steady two-dimensional, three-velocity-component Euler equations (2D-3C) on our domain, allowing its linear stability properties to be investigated for various q (Sec. III). These results are used to interpret, in Sec. IV, the nonlinear interactions that result from fully three-dimensional, three velocity-component (3D-3C) DNS and LES.

II. FLOW GEOMETRY AND FORMULATION

In dimensionless coordinates to be defined subsequently, the incompressible Navier-Stokes equations (NS) are

$$\frac{\partial u_j}{\partial x_j} = 0, \quad \frac{\partial u_i}{\partial t} + u_j\frac{\partial u_i}{\partial x_j} = -\frac{\partial P}{\partial x_i} + \frac{1}{\mathrm{Re}}\frac{\partial^2 u_i}{\partial x_j^2}, \tag{3}$$

and the convection-diffusion equation for a passive scalar c is

$$\frac{\partial c}{\partial t} + u_j\frac{\partial c}{\partial x_j} = \frac{1}{\mathrm{Re}\ \mathrm{Sc}}\frac{\partial^2 c}{\partial x_j^2}, \tag{4}$$

where Re and $\mathrm{Sc}=\nu/D$ are the Reynolds and Schmidt numbers, respectively, D being the scalar diffusivity. Equations (3) and (4) are applied in Cartesian coordinates on a physical domain that is periodic in the x_1 and x_2 directions and extends to infinity in x_3. In what follows we will consider an array of vortices nominally aligned with the x_1 direction, whose centers are initially on the x_2 axis. For computational purposes, the infinite physical domain is stretched onto a periodic computational dimension ($0 \leqslant \eta < 2\pi$) of finite extent using the mapping

$$x_3 = b\cot\left(\frac{\eta}{2}\right). \tag{5}$$

The primitive variables are expanded on this computational space in terms of Fourier basis functions. As discussed by Cain, Ferziger, and Reynolds[17] this results in minimal truncation errors because the mapping contains only zeroth- and first-order wave modes. A consequence of this is that the mapping introduces only a coupling to neighboring wave modes whenever derivative operations are performed, and to two neighboring modes for second derivatives; hence the resulting scheme retains much of the speed and parallelization benefits of the standard pseudospectral method used in box turbulence. Time integration is performed using a stiffly-stable scheme,[18] since it has a larger region of stability than standard Adams-type explicit schemes. At each time step, nonlinear terms are evaluated in physical space using 2/3-rule dealiasing and the parallel FFTW fast Fourier transform package.[19] The code was validated on several test cases relevant to the present study. These include a comparison with the work of Buntine and Pullin[20] on the merger of two-dimensional (2D) counter-rotating vortices and a validation of the correct growth rate and qualitative behavior for the three-dimensional (3D) development of the long-wavelength instability on the Mallier and Maslowe vortex array[21] in the absence of short wave modes.[22]

A. Initial condition: x_2^*-x_3^* plane

The vortex axis is chosen along one of the strictly periodic directions (x_1 direction); however, the presence of a second periodic direction (x_2) in the plane of the vortex results in an array of image flows. The initial condition is derived from the Mallier and Maslowe[21] (MM) vortex, an exact solution of the inviscid Euler equations which is the counter-rotating analog of the Stuart vortex array.[23] Making quantities nondimensional by the choice of a length scale $L^*/2\pi$, where L^* is the x_2^* period of the array and velocity scale Γ^*/L^*, where Γ^* is the circulation of each member of the array, then the streamfunction for the MM vortex can be expressed as

$$\psi(x_2,x_3) = \frac{1}{2}\log\left(\frac{\cosh(Cx_3) - C\cos(x_2)}{\cosh(Cx_3) + C\cos(x_2)}\right), \tag{6}$$

where $C \in [-1;1]$ is the concentration parameter. When $C=0$, $\psi=0$, whilst for $C \to \pm 1$ the streamlines become more circular until the counter-rotating point-vortex array is recovered at $C=\pm 1$. The Reynolds number in (3) and (4) is then $\mathrm{Re}=\Gamma^*/2\pi\nu^*$ and the dimensionless vortex circulation is $\Gamma=2\pi$. The dimensionless vorticity ω_i is

$$\omega_1(x_2,x_3) = -\Delta^2\psi = \frac{(1-C^2)}{4}\sinh(4\psi), \quad \omega_2 = \omega_3 = 0, \tag{7}$$

while the velocity components are

$$u_2(x_2,x_3) = \frac{C^2\sinh(Cx_3)\cos(x_2)}{\cosh^2(Cx_3) - C^2\cos^2(x_2)},$$

$$u_3(x_2,x_3) = -\frac{C\cosh(Cx_3)\sin(x_2)}{\cosh^2(Cx_3) - C^2\cos^2(x_2)}. \tag{8}$$

Figure 1(a) shows the vorticity distribution for the MM vortex array with $C=0.9$. In order to characterize the vortex separation in this array, one must first define a length scale indicative of the vortex size. Studies of the Lamb-Oseen vortex typically choose the radius at which the azimuthal velocity takes its maximum value,[14,15] the distance at which boundaries or other vortices are present being described in terms of this core size. For the MM vortex, however, the streamlines are only cylindrical in the limit $C \to \pm 1$; the straining influence of the array introducing ellipticity. We consider the plane defined by $x_3=0$ and define the core size as the distance r_c from the core of each vortex $x_{2_c}=n\pi$ (n integer) to the location $x_{2_{\max}}$ at which u_3 takes its maximum value. Thus

$$u_{3_{\max}} \equiv u_3(x_{2_{\max}}) = \pm\frac{1}{2\sqrt{1-C^2}},$$

$$r_c = |x_{2_{\max}} - x_{2_c}| = \pm\frac{1}{2}\cos^{-1}\left(\frac{3C^2-2}{C^2}\right). \tag{9}$$

For $C=0.9$ [Fig. 1(b)], $r_c \approx 0.506$. Increasing C decreases r_c and hence increases the separation size, while providing an initial condition that always satisfies the unsteady Euler equations. For the present work, all simulations are performed with $C=0.9$, which corresponds to a separation distance $\approx 6.2\, r_c$.

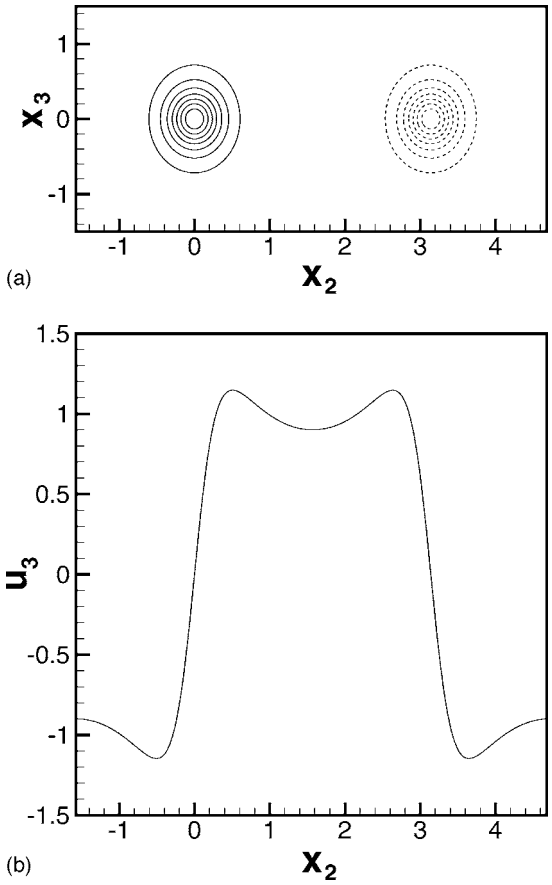

FIG. 1. (a) Contours of ω_1 and (b) distribution of u_3 along $x_3=0$ for the MM vortex with $C=0.9$.

B. Axial velocity

Using (1),(2) can be rewritten in terms of the ratio of the swirling velocity $u^*_{\theta_{\max}}$ to the maximum axial velocity u_d^*

$$q \approx 1.56\frac{u^*_{\theta_{\max}}}{u_d^*}. \tag{10}$$

We retain this definition of q, replacing $u^*_{\theta_{\max}}$ with $u_{3_{\max}}$ and u_d^* with its nondimensional equivalent. An exact solution to the 2D-3C Euler equations can be constructed with any axial velocity distribution that is a function only of ψ. Presently we choose

$$u_1(x_2,x_3) = \frac{1.56u_{3_{\max}}}{q_0}\left|\frac{\omega_1(x_2,x_3)}{\omega_1(0,0)}\right|. \tag{11}$$

Where the subscript in q_0 distinguishes the chosen initial swirl parameter from its transiently varying counterpart [Eq. (10)]. The velocity field defined by (8) and (11) is only a weak solution of the steady 2D-3C Euler equations because the absolute value function introduces a discontinuity in the axial velocity derivative at $x_2=(\pi/2)+n\pi$, for integer n. The presence of viscosity in the full NS simulation will act to

smooth out this discontinuity. Even in the absence of viscosity, the jump in the velocity derivative turns out to be less than 1% of the value at the vortex core when a separation parameter $C=0.9$ is used.

C. Vortex strain

For an array of point vortices, the strain at the center of each vortex is that induced by the array at the vortex position if it were not present. Denoting by a the separation distance between counter-rotating pairs, this can be shown to be $\gamma = \pi\Gamma/12a^2$. For two isolated point vortices, the strain is lower with $\gamma=\Gamma/2\pi a^2$. Moore and Saffman[24] calculated that an exterior imposed strain distorts the Rankine vortex into an ellipse. When the resulting self-induced strain is included[25] for the counter-rotating pair, this results in a total strain at the center of vorticity

$$\gamma = \Gamma/\pi a^2. \tag{12}$$

For the MM initial condition with no axial flow, the equivalent strain rate at $(x_1,x_2)=(0,0)$ is

$$\gamma = \pi C\Gamma/4a^2. \tag{13}$$

These results are useful for later comparison with experiment.

III. STABILITY

Julien, Chomaz, and Lasheras[22] studied the linear stability of the MM vortex without axial flow, finding periodic array analogies to the long- and short-wavelength modes that Crow[4] and Widnall, Bliss, and Tsai[5] found for the two-vortex system. They found that, while the long-wavelength Crow instability is almost independent of Re, viscous action damps the shorter-wavelength modes. Stability analysis of the Batchelor vortex[13] shows that the presence of axial flow introduces helical-mode instabilities for sufficiently low q. To study the effect of axial flow on the stability of the vortex array, we utilize the NS equations linearized with respect to perturbations in velocity u_i' and pressure P' about the base flow u_i defined by (8) and (11).

$$\frac{\partial u_j'}{\partial x_j} = 0,$$

$$\frac{\partial u_i'}{\partial t} + u_i'\frac{\partial u_i}{\partial x_j} + u_j\frac{\partial u_i'}{\partial x_j} = -\frac{\partial P'}{\partial x_i} + \frac{1}{\mathrm{Re}}\frac{\partial^2 u_i'}{\partial x_j^2}. \tag{14}$$

The perturbation field can be written in the form

$$[u_i', P'](x_1,x_2,x_3,t) = \sum_{k_1} [\hat{u}_i', \hat{P}'](k_1,x_2,x_3,t)e^{ik_1x_1}. \tag{15}$$

Since the base flow is independent of x_1, (15) causes (14) to decouple in axial wave space allowing the stability problem to be solved independently at each k_1 simultaneously, using the parallel algorithm. Equation (14) was integrated as an initial-value problem using the same mapping and splitting method used for the nonlinear code. The instability modes are separated into two families, namely, the sinuous mode (antisymmetric) defined by

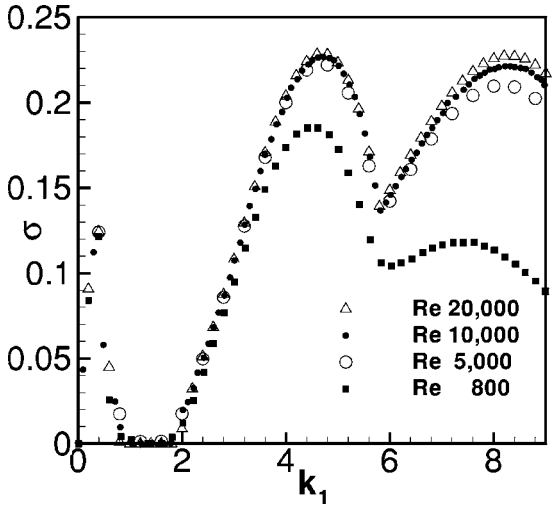

FIG. 2. Growth rate of the antisymmetric modes with no axial velocity ($q_0=\infty$), showing the two regimes. The Crow instability at long wavelengths and the more viscous dependent Widnall instabilities at shorter wavelengths. Filled symbols are taken from the work of Julien, Chomaz, and Lasheras (Ref. 22) at Re of 800 and 10 000. The open symbols are computed from the present study at Re 5 000 and 20 000.

$$[u_1', u_2', u_3'](x_2,x_3,t) = [-u_1,-u_2,u_3](x_1,x_2+\pi,-x_3,t), \tag{16}$$

and the varicose mode (symmetric) by

$$[u_1', u_2', u_3'](x_2,x_3,t) = [u_1,u_2,-u_3](x_1,x_2+\pi,-x_3,t). \tag{17}$$

The initial condition for the divergence-free perturbation velocity field comprises white noise exhibiting each of these symmetry properties, modulated by an exponential decay in x_3.

At each time step the kinetic energy at each axial wavelength k_1 is computed and the perturbation energy E determined by integrating over the x_2-x_3 plane. The integration is carried on in time sufficiently long for the most unstable eigenmode to dominate, as evidenced by convergence of the growth rate defined as[22]

$$\sigma = \lim_{t\to\infty}\frac{1}{2}\frac{d\ln E}{dt}. \tag{18}$$

Figure 2 shows the maximum growth rates at four different Reynolds numbers for sinuous modes at discrete axial wave numbers for $q=\infty$, which corresponds to no axial flow. Two regimes are identified, separated by a region of negligibly small growth rate. The first of these occurs for $k_1<1$ and corresponds to the periodic analogy to the long-wavelength Crow instability mode (CM) with a peak at $k_1\approx 0.4$. The second, for $k_1>2$, is associated with the short-wavelength, Widnall-type instability modes (WM) and shows two distinct peaks. The present study supports the findings of Julien, Chomaz, and Lasheras[22] that the peak CM appears to be viscosity independent, while the WM becomes increasingly affected at higher wave number.

The case of the varicose mode (cf. Julien, Chomaz, and Lasheras[22]) differs from the sinuous in that the imposed symmetries do not allow the Crow instability to develop. The

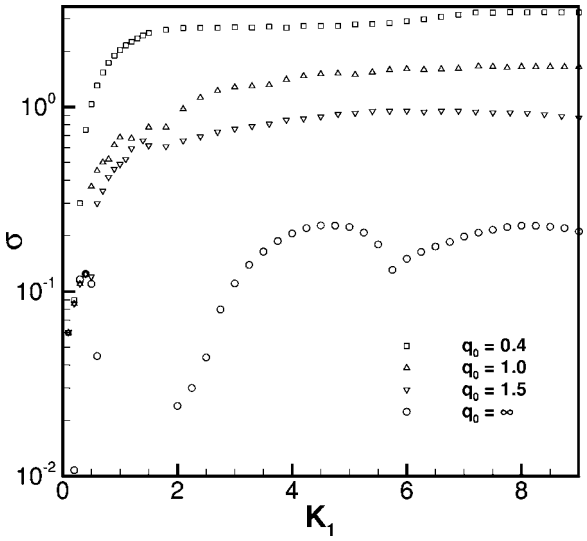

FIG. 3. Growth rate vs axial wave number for the antisymmetric modes of the MM vortex with $C=0.9$ for different values of q_0.

corresponding growth rates in this region are very low. At shorter wavelengths they approach those for the previous case with moderate growth rates observed in the region considered stable to sinuous modes. We can therefore hypothesize that, since viscosity effects are confined to high wave numbers, Re will influence this family of instabilities in the same manner. We conclude that, since little difference is found between the three highest Reynolds numbers, the Re $=20\,000$ case is a good approximation to the limit $\mathrm{Re}\to\infty$. This Re is also of interest as it is near that estimated for the mixing transition to occur.[26]

Figure 3 shows the stability properties when an axial flow, $q_0\neq\infty$, is added to the base flow. It can be seen that the resulting vortex array exhibits larger growth rates due to the additional instability mechanism resulting from the axial flow. As the magnitude of the axial velocity is increased (corresponding to a decrease in q_0) the maximum growth rates increase significantly. Of particular note for the sinuous mode is the point $k_1\approx 0.4$, $\sigma\approx 0.1$, which is in the vicinity of the peak growth rate of the Crow instability. At higher wave numbers the largest growth rates increase with decreasing q and are presumably the periodic analog of the helical instability modes observed for the Batchelor vortex. Finally, it should be noted that modes resulting from the presence of axial velocity exhibit high growth in the region $1<k_1<2$, where insignificant growth of the sinuous modes were observed in the absence of axial flow.

IV. 3D-3C SIMULATIONS

The study of the vortex array is now extended beyond the linear analysis by 3D-3C numerical simulation of the Navier-Stokes equations. To aid the analysis of the DNS and LES presented subsequently, we develop diagnostics for analyzing the flow. We begin by defining by $\langle\phi\rangle$ the integral of the quantity ϕ over the domain

$$\langle\phi\rangle=\int_0^{L_{x_1}}\int_0^{2\pi}\int_{-\infty}^{\infty}\phi(x_1,x_2,x_3)dx_1dx_2dx_3. \tag{19}$$

For all ϕ considered presently, this integral exists. Taking the dot product of (3) with u_i, and integrating over the domain using x_1,x_2 periodicity as well as quiescent flow at infinity, a conservation equation for the volume-averaged kinetic energy $\langle E\rangle$ is obtained

$$\frac{d}{dt}\left\langle\frac{1}{2}u_i^2\right\rangle=-\frac{2}{\mathrm{Re}}\langle S_{ij}S_{ij}\rangle, \tag{20}$$

where S_{ij} is the rate-of-strain tensor and the term on the right represents the viscous dissipation $\langle\epsilon_\nu\rangle$ which can be written

$$\langle\epsilon_\nu\rangle=\frac{1}{\mathrm{Re}}\left\langle\left(\frac{\partial u_i}{\partial x_j}\right)^2\right\rangle. \tag{21}$$

The enstrophy density, $\omega_i\omega_i$, is a measure of the turbulence intensity. It can be shown to be equal to

$$\omega_i\omega_i=\left(\frac{\partial u_k}{\partial x_j}\right)^2-\frac{\partial u_k}{\partial x_j}\frac{\partial u_j}{\partial x_k}. \tag{22}$$

Applying (19)–(22) shows that $\langle\omega_i\omega_i\rangle$ is proportional to the dissipation, and hence is also a measure of the turbulence intensity,

$$\langle\omega_i\omega_i\rangle=\left\langle\left(\frac{\partial u_k}{\partial x_j}\right)^2\right\rangle=\mathrm{Re}\langle\epsilon_\nu\rangle. \tag{23}$$

This is useful when considering LES, where only the resolved-scale enstrophy integral can be calculated. The resolved and subgrid dissipation integrals can be summed to provide a means for estimating the total enstrophy; this sum can also be interpreted as a measure of the turbulence intensity of the flow. Finally, as a measure of the intensity of each vortex, we define by $\bar{\Gamma}$ the circulation around one positively signed vortex in the array, averaged in the axial direction

$$\bar{\Gamma}=\frac{1}{L_{x_1}}\int_0^{L_{x_1}}\int_{-\pi/2}^{\pi/2}\int_{-\infty}^{\infty}\omega_1(x_1,x_2,x_3)dx_3dx_2dx_1. \tag{24}$$

Two techniques are used for flow visualization, the first of which is based on the local velocity field around a critical point.[27] To linear order, this is governed by the velocity gradient tensor $\partial u_i/\partial x_j$. For an incompressible flow, the eigenvalues λ of $\partial u_i/\partial x_j$ are calculated from

$$\lambda^3+Q\lambda+R=0, \tag{25}$$

where

$$Q=-\frac{1}{2}[S_{ij}S_{ji}+\Omega_{ij}\Omega_{ji}] \tag{26}$$

and

$$R=-\frac{1}{3}[S_{ij}S_{jk}S_{ki}+3\Omega_{ij}\Omega_{jk}S_{ki}] \tag{27}$$

are the second and third invariants of $\partial u_i/\partial x_j$, and S_{ij} and Ω_{ij} are the symmetric and antisymmetric parts of the velocity gradient tensor, respectively. $Q>0$ implies a pointwise dominance of rotation over the strain magnitude, and hence

provides a means to identify vortical structures.[27,28] The present base flow has strong background rotation associated with the vortices, and hence is characterized by mostly positive values of Q. For this reason isosurfaces at discrete $Q>0$ are chosen to provide the visualization of the resulting structures. Furthermore, the presence of this strong base rotation is the reason more sophisticated techniques incorporating pressure minima (due to our base flow, the pressure should be lower than ambient everywhere), which have been successfully used for detecting structures in box turbulence,[29,30] were not utilized. The second means of visualizing the flow is through the passive scalar concentration c. The initial condition for c takes the same form as the vorticity in (7), and is intended to be representative of the diffusion of particles or die injected down the core of each vortex. We choose Sc=1, so that no extra resolution requirements are imposed on the DNS.

A. Direct numerical simulation results

A direct numerical simulation (DNS) of the MM vortex both with and without axial flow was performed at Re $\equiv\Gamma^*/2\pi\nu^*=1000$. The axial extent of the domain is set to contain a single wavelength of the most unstable Crow mode. Each vortex in the array (i.e., the half domain) is resolved with $64\times64\times128$ points, the initial core being described by 24 points in the diameter. The base flow is perturbed with divergence-free random noise exponentially decaying with x_3, and the NS equations integrated in time. The time step is chosen such that the initial Courant-Friedricks-Lewey (CFL) number is 0.1. The various flow regimes resulting throughout the development of both the $q=\infty$ and $q=1$ initial conditions are analyzed by considering the evolution of the integrated quantities $\langle E\rangle,\langle\epsilon\rangle$, and $\bar{\Gamma}$ in Fig. 4(a) and 4(b) as well as through snapshots of the flow at several stages in Fig. 5. Visualization is through an isosurface of $Q=1$ shaded by local dissipation ϵ.

1. Early development

Figure 5(b) shows that, consistent with the linear stability study, the destabilizing effect of axial flow causes the initial perturbations to grow at a faster rate than in its absence; helical structures with wave number $k_x\approx2$ accompanied by regions of increased dissipation are observed to develop on each vortex in the array. The linear stability study found a local maxima in the growth-rate versus axial wavenumber curve (Fig. 3) at around this wavelength. Viscosity most likely damps the higher-growth-rate, shorter-wavelength modes in the viscous DNS. In Fig. 4(a) it can be seen that globally, this leads to a slight increase in the volume-averaged dissipation and a corresponding faster decay of kinetic energy. As expected, the averaged circulation is unaffected by the axial velocity since its destabilizing effect acts on each vortex independently and does not lead to enhanced intervortex vorticity convection. During this initial phase, the evolution of each vortex is qualitatively similar to that of an isolated vortex, and is best described in cylindrical components. Figure 6 shows that, similarly to the isolated case, the maximum axial velocity shows a sharp decrease

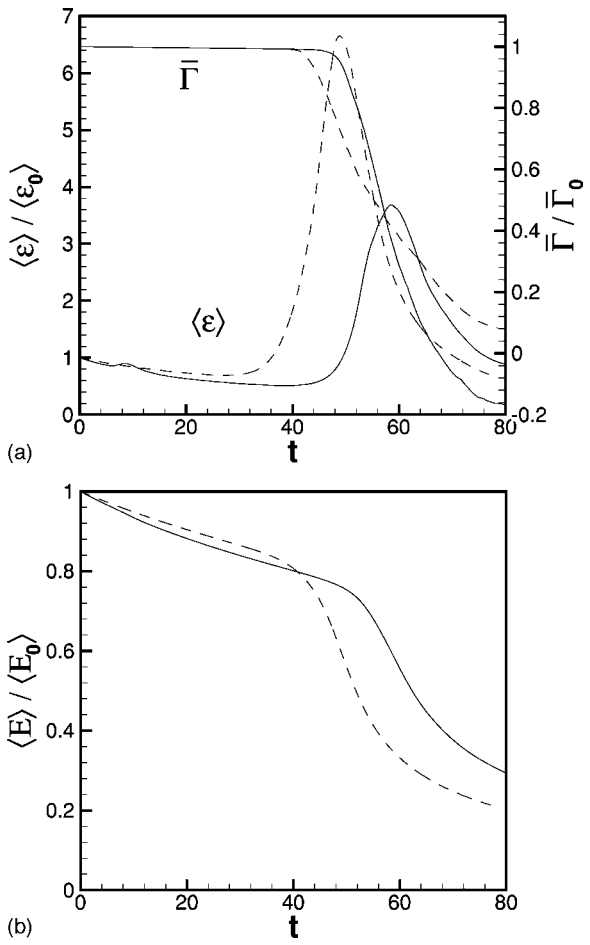

FIG. 4. Evolution of volume integrated quantities for the DNS of the Re $=1000$ MM vortex with $C=0.9$ for $q_0=1$ (solid lines) and $q_0=\infty$ (dashed lines). (a) dissipation and circulation (b) normalized energy.

initially while the azimuthal component maintains a constant gradual decay. Presumably, the mechanism is the same as for the Batchelor vortex studied by Jacquin and Pantano,[16] whereby the energy of the axial flow is extracted by turbulence within the core, the perturbations generated being transported outward toward regions of local stability where they don't modify the mainly tangential flow. Consequently, q increases and in keeping with the linear analysis the vortex evolves through regimes of progressively weaker instability rates. Ultimately, the core stabilizes with respect to the helical modes and the vortex relaminarizes before the cooperative modes have shown appreciable growth.

2. Cooperative instabilities

At slightly later times, Fig. 5(d) shows that small-amplitude kinks begin to become apparent in both the $q_0=\infty$ and $q_0=1$ cases. These are a result of the more slowly growing higher-order Kelvin modes predicted by linear stability. As these modes grow, the periodic analog of the long-wavelength Crow instability appears, bending the vortices such that sections move alternately toward and away from each neighbor. In Fig. 5(e), ($t=40$), a striking difference between the two flows has become apparent. In the absence of axial velocity, the WM has distorted each vortex to the extent

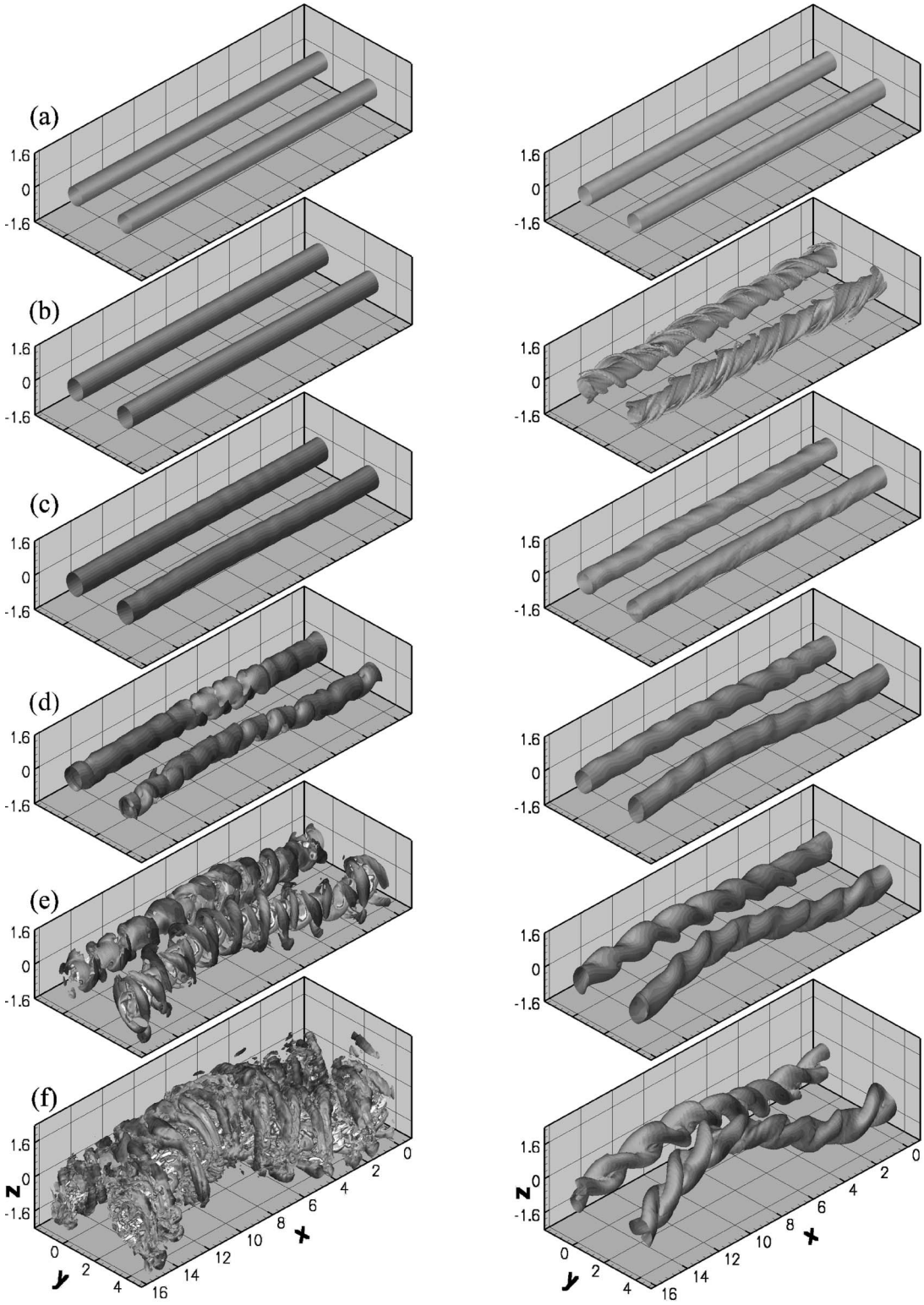

FIG. 5. Flow visualization comparison through an isosurface with $Q=1$ on which contours of dissipation are plotted for the Re 1 000 DNS of the $C=0.9$ MM vortex with $q_0=\infty$ left and $q_0=1$ right. Evolution is from top to bottom and shown at nondimensional times (a) 0, (b) 12, (c) 20, (d) 32, (e) 40, and (f) 45.

that separate tubular structures can be seen surrounding a highly dissipative core region. The next snapshot captured in Fig. 5(f) shows that, analogous to the vortex-pair experiments of Leweke and Williamson[25] (LW henceforth), the fluid in these structures is drawn closer to the neighboring vortices where it is quickly wrapped around by the mean circulation. This effect is magnified in regions where the CM pulls pairs of vortices closer together, increasing the local strain, and hence the WM growth rate. Ultimately this exchange of fluid between counter-rotating pairs results in a

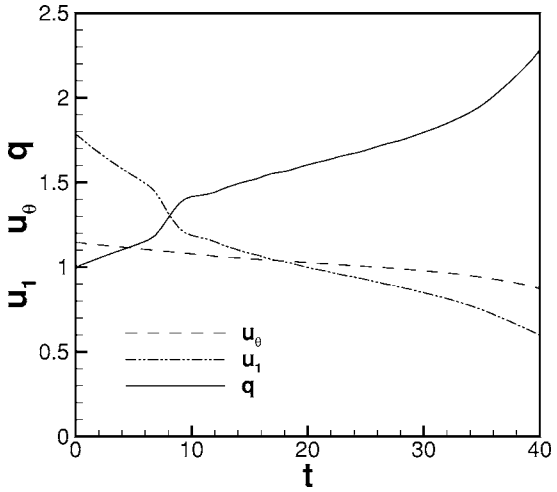

FIG. 6. Evolution of the maximum axial and azimuthal velocity components as well as the swirl parameter for Re=1000.

rapid decrease in circulation and an explosive growth in dissipation. In contrast, the helical structure that results from the axial velocity is observed to persist. While the WM is still present, the flow appears to be more resistant to the aforementioned phenomenon. This is seen from the volume-averaged quantities in Fig. 4, where the onset of both the sharp decrease in circulation and growth in dissipation are delayed.

At later times the dissipation peaks in both cases before undergoing a rapid reduction, in accordance with the significant cancellation of opposite-signed vorticity. This maxima is significantly higher for the $q_0=\infty$ case, providing further evidence of the increased short-wavelength interactions that occur in the absence of axial flow. As pointed out by LW, the final state is different from the organized array of vortex rings that would result from the reconnection of the primary structures if only the CM were present. The presence of the WM enhances transport, and hence the redistribution of energy from the large-scale structures to the small scales where it is dissipated. In the case of the vortex pair, Fig. 23(d) of LW shows that the flow evolves to a state of periodic regions of small-scale motion separated by thin vortical structures. The authors suggest that this is a result of a pressure gradient between regions where the primary vortex is intact and where it has broken up due to the CM bringing the pair closer together (resulting in pressure relaxing towards the ambient as discussed by Saffman[31]); the axial velocity that results transports fluid away from the latter region leaving "skeletons of the initial vortex pair." For the periodic case one would expect a similar behavior over a shorter wavelength as the CM pulls each vortex alternately closer to both neighbors. Plots of passive scalar concentration in Figs. 7 and 8 show this phenomenon beginning to occur where regions of higher concentration can be seen at the points of zero-amplitude displacement of the CM. Visual comparison with the experiments at later times was not possible because simulation with the high Schmidt number of dye could not be performed, owing to computational resolution constraints; at Sc=1, fast diffusion makes effective visualization difficult.

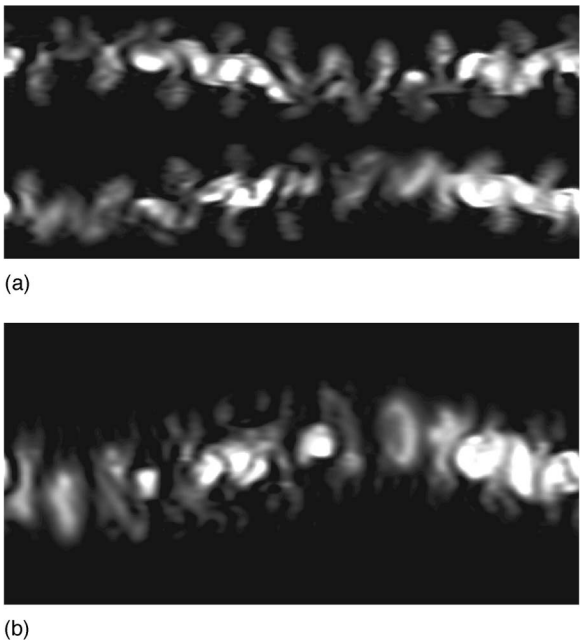

FIG. 7. Contours of passive scalar for the Re=1000, $q_0=\infty$ MM vortex at time 45 on slices through the core of the vortex in the *xy* plane (a) and the *yz* plane (b).

3. Circulation

LW computed the circulation evolution around sections of one vortex in planes where the pairs are brought closer together and where they are separated. The important time scale for this phenomenon is the reciprocal of the strain rate felt at the center of each vortex produced by all neighbors. This determines the growth rate of the WM instabilities. As discussed in Sec. II C, this strain takes the value given by

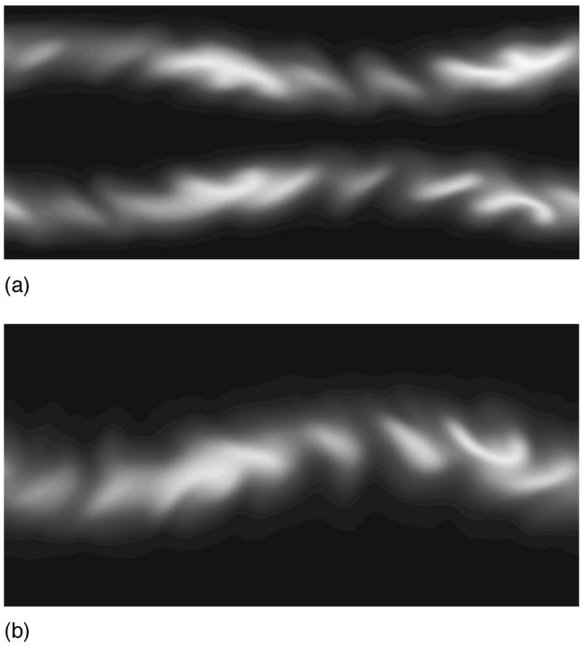

FIG. 8. Contours of passive scalar for the Re=1000q_0=1 MM vortex at time 45 on slices through the core of the vortex in the *xy* plane (a) and the *yz* plane (b).

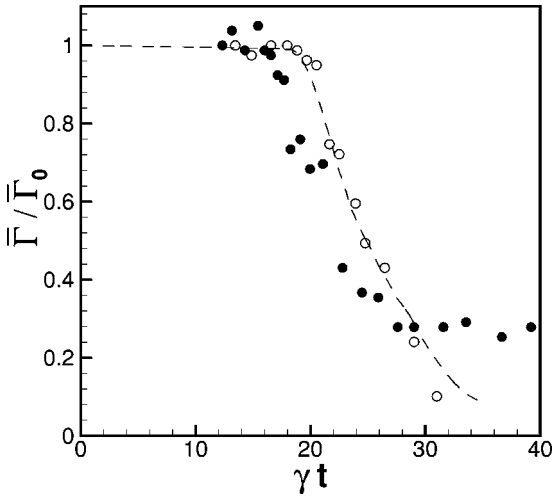

FIG. 9. Circulation comparison with the experiments of Leweke and Williamson (Ref. 25) (Fig. 26), with abscissa rescaled to the present nondimensionalization and shifted to coincide. The solid circles represent data in a plane where the vortices are brought closer together and the open symbols where they are separated. The dashed line is the averaged circulation for the $\mathrm{Re}=1000, q_0=\infty$ case.

(12) and (13) for the case of the vortex pair and the MM vortex array, respectively. Figure 9 shows $\bar{\Gamma}$ vs γt for $q_0=\infty$ compared with the experimental points of LW, with the abscissa shifted such that the onset of the circulation decay occurs at about the same time. Good agreement is observed for the initial period of decay, where the rate is approximately the same in both experimental planes. At later times, the circulation flattens off when the skeleton vortices appear where the CM brings the pair closer together, and continues to decrease in regions identified as consisting of small-scale motion. The decay rate of $\bar{\Gamma}$ decreases at this time, which is consistent when viewed as an average of these two phenomena. By this late time, the enstrophy level has returned almost to initial levels and the energy has decreased by a factor of 5.

4. Alignment statistics

We now consider the statistics of alignment between the eigenvectors of S_{ij} and ω_i, the former being denoted by $(\hat{e}_i^1, \hat{e}_i^2, \hat{e}_i^3)$ ordered according to the corresponding eigenvalues $(\lambda_1, \lambda_2, \lambda_3)$, with $\lambda_3 > \lambda_2 > \lambda_1$ and $\lambda_1+\lambda_2+\lambda_3=0$. We determine the probability density function (pdf) of alignment between a vector and a symmetric tensor in a 3D coordinate system.[32] Local coordinates are used, defined by the orthogonal eigenvectors of S_{ij}, ω_i being described through its polar angle θ and azimuthal angle ϕ relative to $\hat{e}_i^3$ and $\hat{e}_i^2$, respectively. There is no distinction between angles in the range $(0, \pi/2)$ and $(\pi/2, \pi)$. Joint pdfs of ϕ and $\cos(\theta)$ are computed. Because the present study is conducted on a domain of infinite physical extent on which the volume coverage of turbulent flow is zero, the pdfs are presented thresholded on dissipation exceeding 10% of its maximum.

Results obtained at six time instances (corresponding to those in the visualization in Fig. 5) are shown in Fig. 10 for the case $q_0=1$. While the $q_0=\infty$ initial condition corresponds to a delta function pdf at $\phi=0$, $\cos(\theta)=0$, the presence of axial velocity leads to a more widely distributed band of alignment as shown in Fig. 10(a). The particular shape and location of the correlation between ϕ and θ is characteristic of an initial axial flow that results in all components of the rate of strain tensor being of the same order of magnitude. As the flow develops through the previously mentioned stages, Figs. 10(b)–10(e) show that the preferred alignment shifts toward smaller values of ϕ and $\cos(\theta)$. By time $t=45$, it can be seen from Fig. 10(f) that the flow has evolved to a state in which the vorticity vector aligns itself preferentially with the eigendirection corresponding to the intermediate eigenvalue of S_{ij}. This tendency is similar to that observed in previous studies of isotropic turbulence.[32,33]

5. Effect of resolution and domain size

Since the flow exhibits no true homogeneous directions, meaningful spectra are difficult to compute, and so a different test of resolution is required. We consider (20) which is satisfied exactly if the DNS is fully resolved. Figures 11(a) and 11(b) show a comparison between the terms in this equation and the resulting relative error as the simulation progresses. For most of the simulation, the error is very small; however, at later times it increases to the order of 1%. This is most likely due to the CM pulling the vortices in the x_3 direction into regions where the grid is coarser. While this indicates that the simulation is not fully resolved at late times, the error is small, especially when one considers that dissipation takes place at the small scales. To test this, simulations were performed using twice as many modes in x_3 while maintaining the same core resolution. This has the effect of increasing the resolution at larger x_3 values and resulted in an error reduction of an order of magnitude at times when the long-wavelength modes distort the vortices into these regions. For both cases, with and without axial flow, no discernible differences were seen in the observed phenomena during the time period of interest.

Another effect that must be considered is the influence of the axial domain size, since this imposes a periodicity onto the solution, restricting the spectrum of permissible instability modes. While this is a fundamental problem with the temporal approach, simulations on a domain twice as long axially showed very similar results. This simulation still does not capture all the long-wavelength modes; however, it is felt that the main role that this instability plays is in bringing parts of vortex pairs sufficiently close for vortex disintegration to initiate via the short-wavelength modes.

B. Large-eddy simulation

The physical space formulation of the stretched-vortex subgrid scale model[34] is used to enable large-eddy simulation (LES) to be performed at what theoretically could be arbitrarily high Reynolds numbers. In this model, it is assumed that subgrid motion is that produced by straight, nearly axisymmetric vortices, the resulting subgrid stresses being

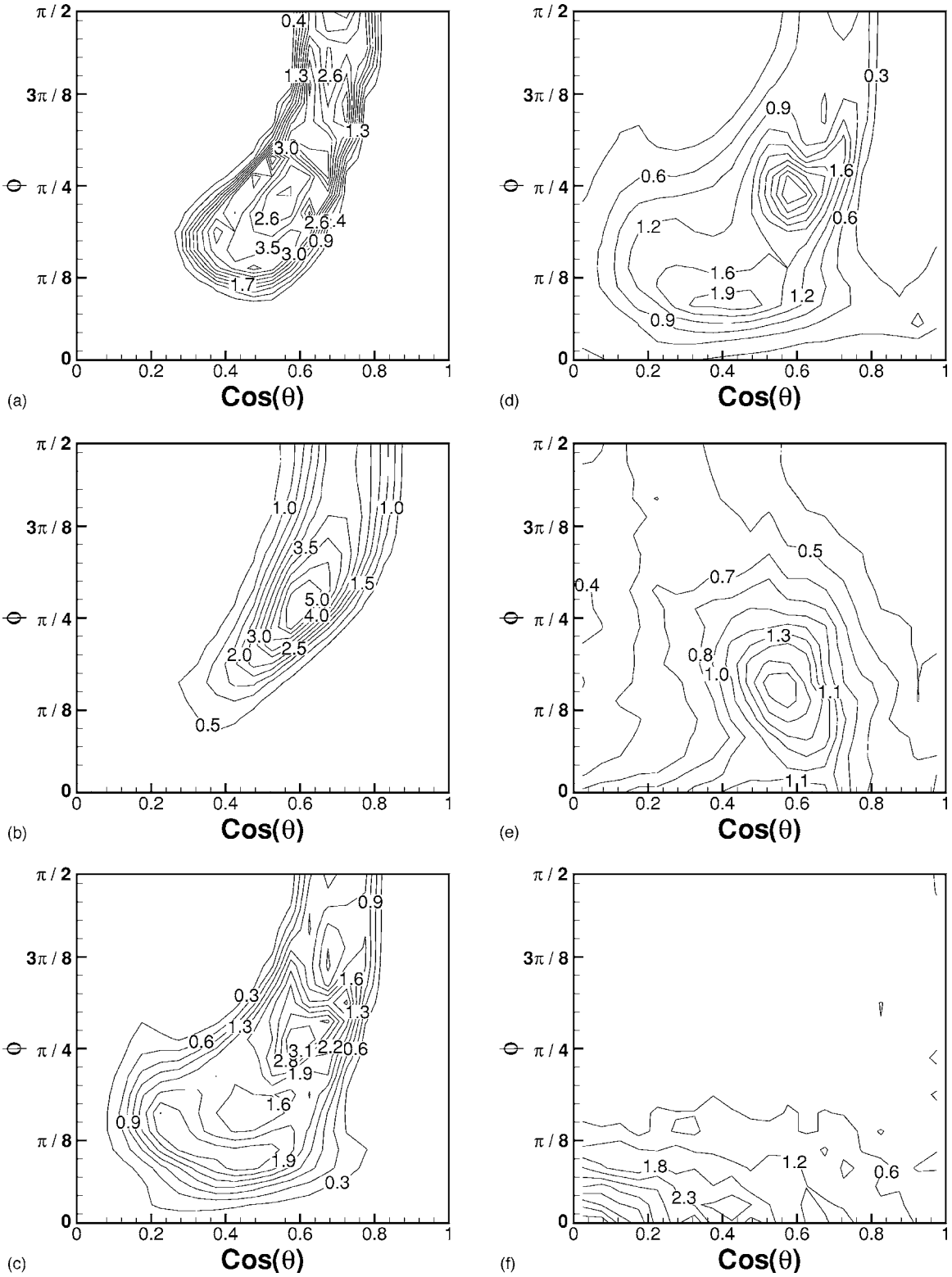

FIG. 10. Joint pdf of the alignment between the vorticity vector and the eigenvectors of S_{ij} for $q_0=1$ at (a) $t=0$, (b) $t=12$, (c) $t=20$, (d) $t=32$, (e) $t=45$, and (f) $t=50$. 20×20 bins of equal widths in each direction are used to compute the pdfs.

$$[\tau_{ij}]_{\mathrm{mod}} = K(\delta_{ij} - e_i^v e_j^v), \quad K = \int_{k_c}^{\infty} E(k)dk, \tag{28}$$

where e_i^v is the unit vector of the subgrid vortex axis, and the subscript "mod" indicates that the term represents a modeled quantity. The subgrid turbulent kinetic energy (TKE) is estimated by assuming that subgrid vortices are Lundgren spirals[35] with subgrid energy spectrum

$$E(k)_{\mathrm{mod}} = \mathcal{K}_0 \epsilon^{2/3} k^{-5/3} \exp[-2k^2\nu/(3|a|)], \tag{29}$$

where $\mathcal{K}_0$ is the Kolmogorov prefactor, ϵ is the local cell-averaged dissipation (resolved flow plus subgrid scale), a

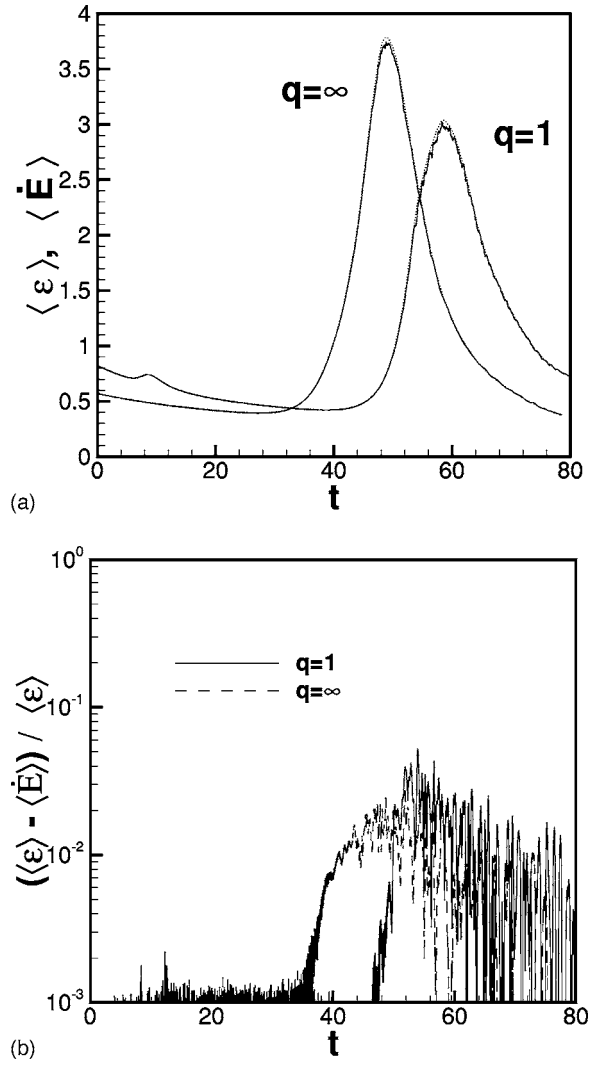

FIG. 11. Resolution measurements for the Re=1000 MM vortex with $C=0.9$ for $q_0=1$ and $q_0=\infty$ (a) rate of change of kinetic energy compared to dissipation. (b) Relative error between the two.

$=S_{ij}e_i^v e_j^v$ is the axial strain along the subgrid vortex axis provided by the local resolved flow, and S_{ij} is the rate of strain tensor of the resolved flow. The pdf that governs the alignment of the subgrid structures through e_i^v, is chosen to distribute proportionally between the direction of the vorticity vector e_i^ω and that of the most extensional eigenvector of the rate of strain tensor $\hat{e}_i^3$,

$$P(e_i^v) = \mu\wp(e_i^v|\hat{e}_i^3) + (1-\mu)\wp(e_i^v|e_i^\omega), \tag{30}$$

where $\wp(e_i^v|e_i)$ is the delta function probability density that e_i^v is aligned with vector e_i. Presently we use the model ansatz

$$\mu = \frac{\lambda_3}{\lambda_3 + \sqrt{\omega_i\omega_i}}. \tag{31}$$

This alignment model allows backscatter and has performed excellently on simulations of isotropic turbulence and Channel flow.[36] Physically, this is motivated by a compromise between $\mu=1$, which represents the correlation of the small-scale vorticity with the overall intermediate principal rate of strain (this includes the strong local strain rate provided by the subgrid vorticity), and $\mu=0$ corresponding to the alignment of the subgrid vortex with ω suggested by the idea of small scales generated through the instability of larger structures. Finally, a tractable model is obtained by determining the product $\mathcal{K}_0\epsilon^{2/3}$ in (29) locally using an estimate of the local second-order velocity structure functions obtained from the six-point stencil around each cell.[36,37] For analysis purposes, the total dissipation integral for LES runs is computed as

$$\langle\epsilon\rangle = \langle\epsilon_\nu\rangle + \langle\epsilon_{\text{sgs}}\rangle, \tag{32}$$

and interpreted as a measure of the turbulence intensity in accordance with (23).

1. Flow evolution summary

Initially, simulations were performed at Re=20 000 because this is approximately where a mixing transition is proposed to occur,[26] with fully developed turbulence for higher Re. Again, the axial extent of the domain is set to contain the unit wavelength of the most unstable Crow mode. Each vortex in the array (1/2 domain) is resolved by $64\times64\times256$. The initial core still contains 24 points across its diameter, with the additional resolution in the x_3 direction included to reduce truncation errors associated with the grid-stretching function.

Figure 12 shows a comparison of the evolution of $\langle\epsilon\rangle$ and $\bar{\Gamma}$ for $q=\infty$ and $q=1$. Flow visualization through isosurfaces of $Q=5$ shaded with dissipation at several snapshots is displayed in Fig. 13. As in the DNS, the presence of axial flow initially causes each vortex to develop helical instability modes leading to increased levels of turbulence. At the larger Re of the LES, the growth in dissipation is greater and, despite the weakening of the instability mechanism, it fails to drop to its original level before the cooperative instabilities take over. As observed in the DNS, the effect of axial velocity is to prolong the onset of vortex disintegration. For the LES the delay is longer, presumably due to the greater intensity of the helical structure within each vortex.

2. SGS model performance

The performance of the subgrid model is shown in Fig. 12(d) through the dissipation ratio ϵ_{ratio} defined as the proportion of the total dissipation that comes from the subgrid

$$\epsilon_{\text{ratio}} = \frac{\langle\epsilon_{\text{sgs}}\rangle}{\langle\epsilon_\nu\rangle + \langle\epsilon_{\text{sgs}}\rangle}. \tag{33}$$

It can be seen that, as expected, the model is most active during the WM phase where the circulation decay occurs and in the case of axial velocity, the period of initial helical growth. At its peak, the model contributes approximately 70% of the total dissipation in both cases. It is interesting to note that this is roughly the same as for the channel flow simulations of Veolkl, Pullin, and Chan[36] at $\text{Re}_\tau=1017$, which corresponds to a large scale Reynolds number (based on centerline velocity) of around 20 000. While the macroscopic details of the two flows are quite different, the small-scale details appear to be similar. Toward the end of the simulation, when the circulation decay is complete, the sub-

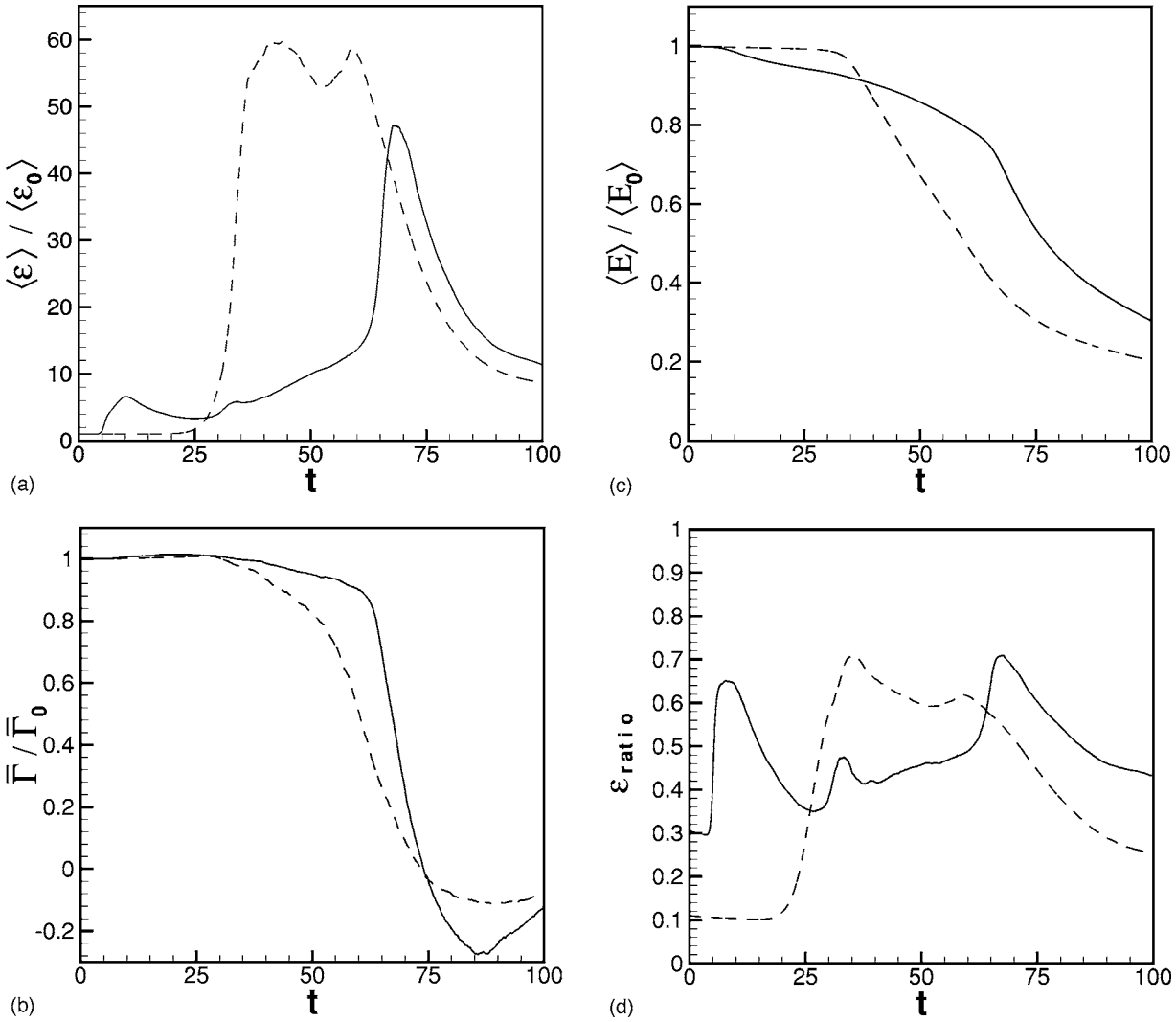

FIG. 12. Evolution of (a) dissipation, (b) circulation, (c) energy, and (d) ϵ_{ratio} for Re=20 000 with $q_0=1$ (solid lines) and $q_0=\infty$ (dashed lines).

grid contribution diminishes indicating that the flow is becoming more resolved.

To gain further insight into the performance of the model, we consider the alignment statistics between the eigenvectors of S_{ij} and the eigenvectors of the subgrid stress tensor. Tao, Katz, and Meneveau[32] computed such alignment pdfs from their experiments of fully developed turbulent flow in a duct by filtering their data to obtain resolved and subgrid scales. While it may be unreasonable to expect a subgrid model to reproduce these pdfs accurately, we note that the average angle between the most extensive stress and the most extensional rate-of-strain is approximately 39°, which is near the preferred alignment angle of 34° found from the experimental study.

3. Early development

Figure 14 shows, for $q=1$, the evolution of $\langle\epsilon\rangle/\langle\epsilon_0\rangle$ during this period for Reynolds numbers in the range 1000–20 000. It can be seen that as Re is increased, so too do both the dissipation growth rate and the peak dissipation level obtained. After this maxima, the dissipation decreases at a rate that is approximately independent of the Reynolds number. At later times the cooperative instabilities dominate as seen in the DNS; the CM pulls vortex pairs together, where enhanced transport via the short-wavelength instabilities leads to the eventual disintegration of the vortex. The linear analysis suggests that the long-wavelength modes, and hence the time scale for initiation of this phenomena, are independent of Re. We conclude that complete relaminarization of the vortex is not observed at the higher Reynolds number, as in the isolated vortex simulations of Sreedhar and Ragab,[15] because insufficient time passes for the smaller viscosity to damp out the turbulent fluctuations prior to the dominance of cooperative instabilities.

As with the DNS, the early evolution of each vortex behaves as if unaffected by the dynamical influence of members of the array. It is therefore useful to speak in terms of cylindrical velocity components. Furthermore, radial distributions are obtained by averaging over the azimuthal direction. The distribution of circulation thus computed is shown in Fig. 15. It can be seen that, in accordance with the universal inner region of Hoffman and Joubert[9] for turbulent vortices, a region of solid-body rotation develops in the core of the vortex, followed by a transition to a region where the

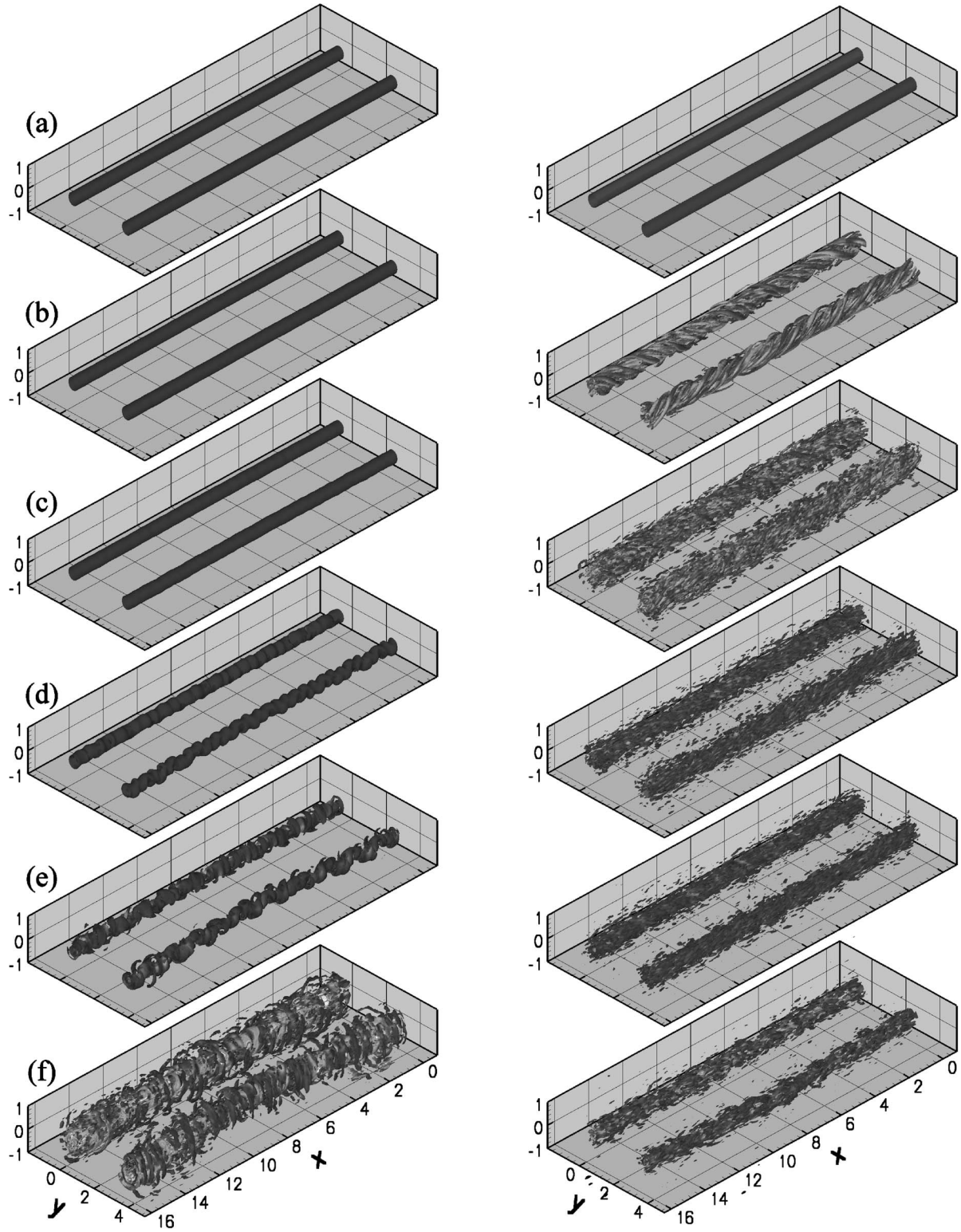

FIG. 13. Flow visualization comparison through an isosurface with $Q=5$ on which contours of dissipation are plotted for the Re 20 000 LES of the $C=0.9$ MM vortex with $q_0=\infty$ left and $q_0=1$ right. Evolution is from top to bottom and shown at nondimensional times (a) 0, (b) 6, (c) 11, (d) 20, (e) 26, and (f) 32.

circulation varies logarithmically. Phillips[38] considered the logarithmic region as only the limiting form for $r=r_c$ and formulated a similarity solution for the approximate form of the circulation as a function of radii for the turbulent trailing vortex. Good agreement is found with the current work up to a radii of approximately $3r_c$, beyond which the influence of the counter-rotating pair becomes substantial. Plots of the cylindrically averaged velocity and ϵ_{ratio} are shown in Fig. 16 for Re=20 000. As expected, the axial velocity maintains its initial bell-shaped profile, although its magnitude in the core

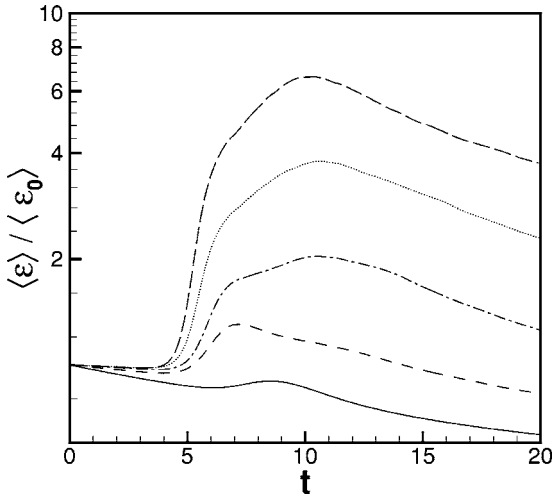

FIG. 14. Effect of Re on the early development of the vortex array with $q_0=1$. Dissipation is plotted at Reynolds numbers 1000, 2000, 4000, 8536, and 20 000 (lower curve to upper curve). The first three were obtained from DNS and the latter two from LES.

decreases as it feeds turbulence generation in that region. Outside the core, however, the axial velocity remains relatively unchanged. In sharp contrast to this, the model dissipation changes only slightly near the center, but becomes more active with time at larger radii, as turbulent fluctuations generated in the core propagate outwards. It is interesting that the model contribution does not die off at small radii, where the turbulent vortex is thought to be a region of laminar solid-body rotation. While this appears to be true in an averaged sense, as is evident in the circulation profile in Fig. 15, we see that, in agreement with previous simulations,[15] the inner region is characterized by high local fluctuations. This is also in keeping with the linear theory, which predicts zero growth rate of short-amplitude disturbances only at the vortex center.[16]

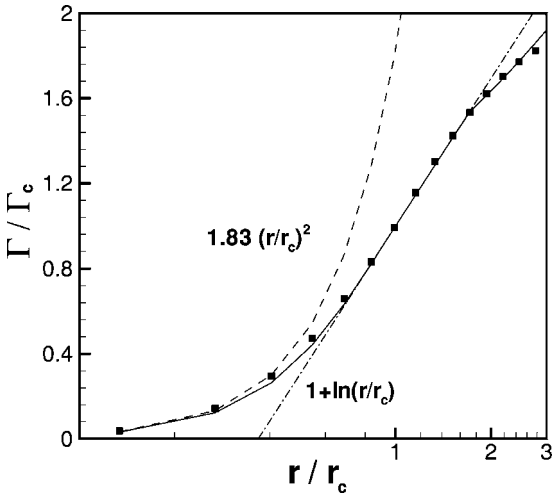

FIG. 15. Circulation profile for Re=20 000 at $t=10$ showing good agreement with the similarity solution of Phillips (Ref. 38) (solid line). Also shown are the inner and logarithmic regions predicted by Hoffman and Joubert (Ref. 9).

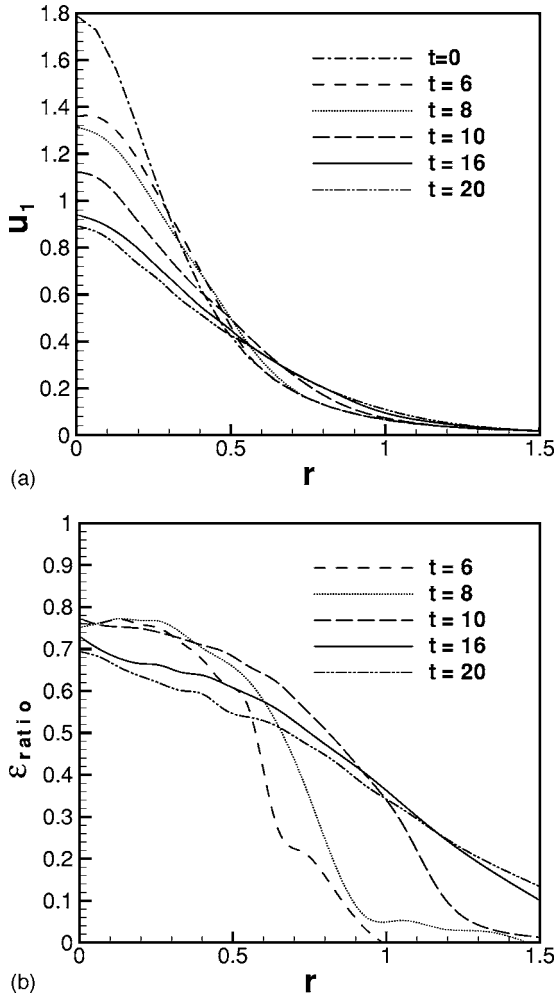

FIG. 16. Radial distributions of (a) the θ averaged axial velocity and (b) ϵ_{ratio} at several instances in time for $q_0=1$, Re=20 000.

4. Mixing transition

In their shear-layer experiments, Konrad[39] (cf. Breidenthal[40]) observed that, above a particular value of the

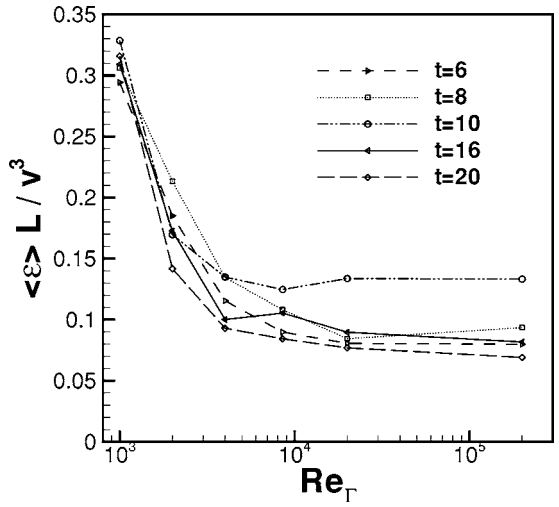

FIG. 17. Dissipation normalized by the maximum swirl velocity and its radial location vs Re at several instances in time.

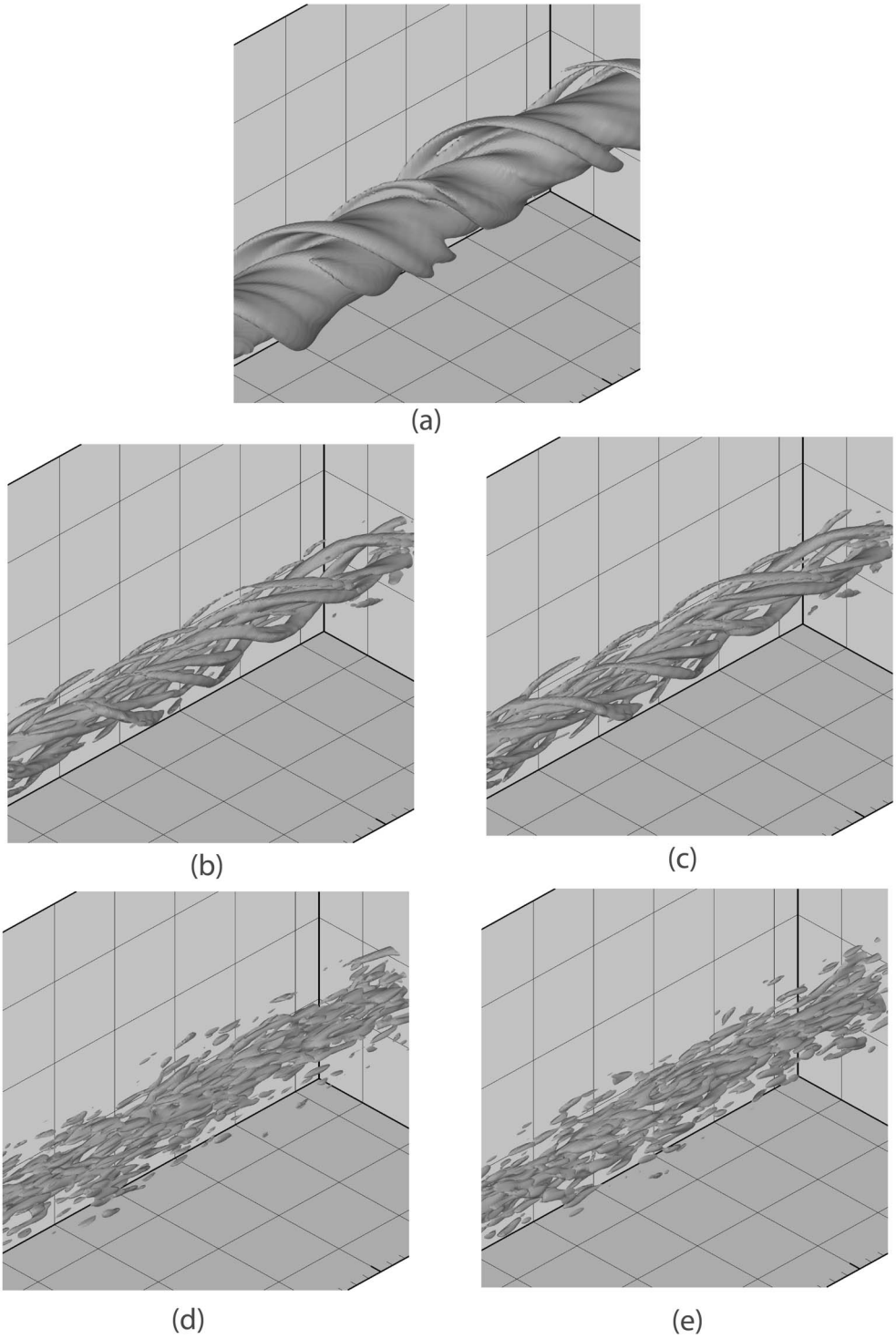

FIG. 18. Enlarged views of a section of one vortex in the array showing the effect of Re on the flow structure through an isosurface of Q. (a) $Re=1000$, $Q=1$, $t=12$. (b) and (c) $Q=5$, $t=6$, Re=20 000, and Re=200 000, respectively. (d) and (e) $Q=5$, $t=10$, Re=20 000 and Re=200 000, respectively.

local Reynolds number, the amount of small-scale mixing increased substantially. Dimotakis[26] generalized this idea to other flows, proposing that above a critical Reynolds number, the flow transitions to a more well-mixed fully developed turbulent state. This mixing transition takes place beyond the usual transition from laminar to unsteady flow that can often be understood in terms of hydrodynamic stability arguments. In shear layers, for example, it is observable as a well-identified transition in the flow, but is less conspicuous in other flows such as jets which are three-dimensional even at low Reynolds numbers.[26] A mixing transition in such flows is qualitatively identifiable through a Reynolds number independence of quantitative measures such as the scalar variance and viscous dissipation. Motivated by results from experiments and DNS of homogeneous turbulence in a spa-

tially periodic cube,[41,42] we now consider the effect of Re on $\langle\epsilon\rangle$ as one means of identifying a mixing transition during the early evolution of the vortex array.

Presently, velocity and length scales, v^* and L^*, are chosen as the (time-dependent) maximum azimuthal velocity component and the radial location at which it occurs. Figure 17 shows the dissipation nondimensionalized in this way versus Re at several stages of the turbulent development initiated by the helical-instability mechanism. The energy dissipation rate appears to be independent of viscosity at high Re. Furthermore, for $\mathrm{Re} \geqslant (1-2)\times 10^4$, it asymptotes to a value of approximately 0.1; somewhat higher at $t=10$. While this constant is generally recognized as a function of the flow geometry, the mixing-transition concept suggests that the Reynolds number above which it is reached is not. By considering experimental and numerical simulation data on a wide variety of flows, Dimotakis[26] concludes that a mixing transition occurs above a large-scale Reynolds number of between $(1-2)\times 10^4$. To support this hypothesis, the Reynolds number dependence on the vortex structure of the flow field is studied by considering isosurfaces of Q (close ups of Figs. 5 and 13). Figure 18(a) and 18(e) shows that while considerable difference is observed between Re=1000 and 20 000, the structure remains almost unchanged when the Reynolds number is raised by an order of magnitude. Two time instances have been shown for the lower viscosity cases to visualize the helical structure developing into smaller-scale motions. This suggests that the mixing transition in the present flow occurs by $\mathrm{Re}=2\times 10^4$, and that the flow field at this value is representative of what would be obtained at all higher Re.

V. CONCLUDING REMARKS

This study has focused on a model for the trailing-vortex wake comprising an array of counter-rotating structures with a superposed axial velocity representative of the roll-up process. The particular form of the initial condition chosen is an exact solution of the 2D-3C steady Euler equations on a domain of infinite extent perpendicular to the plane of the array, thus enabling the linear stability properties to be investigated. We find that, in addition to the slowly growing cooperative elliptic instabilities, the presence of sufficient axial flow leads to modes with significantly higher growth rates. DNS show these modes to be helical in nature, and they appear confined to each structure independent of the array. In agreement with theoretical predictions and previous DNS of a model of an isolated trailing vortex, the turbulence generated as a result of these modes decays, leading to eventual relaminarization owing to a reduction in the axial flow, and hence the underlying instability mechanism. At later times the cooperative instabilities take over. The periodic analog of the Crow instability pulls portions of each pair together, where the disintegration of the vortex is initiated via interactions caused by the short-wavelength Widnall modes. Despite causing higher initially linear growth rates, the presence of axial flow results in structures that appear to resist this breakdown phenomenon for longer periods than for vortices without axial flow. Analysis of the pdfs of alignment between the vorticity and the eigenvalues of the rate of strain tensor show an evolution from an organized state initially towards a final state in which preferential alignment with the intermediate eigenvector is observed. This is similar to what is seen for isotropic turbulence and is further evidence that breakdown has occurred rather than the reconnection expected in the absence of the Widnall modes.

These trends were investigated at higher Reynolds numbers by LES using the stretched-vortex subgrid model. Again, two fundamentally different regions are identified. While the turbulence in each vortex generated by instabilities associated with fast axial velocity decreases significantly, relaminarization is not observed. This suggests that significant growth of the cooperative modes occurs before the lower viscosity has damped out the weakening helical modes. This configuration delays the onset of vortex disintegration longer than at lower Reynolds number. By plotting the dissipation nondimensionalized by the vortex core radius and velocity versus Reynolds number, a mixing transition was identified at $\mathrm{Re}=(1-2)\times 10^4$. This indicates that, beyond this threshold, the flow is less influenced by the Reynolds number, an idea supported by flow visualization at large and intermediate scales.

ACKNOWLEDGMENTS

The authors (J.M.F. and D.I.P.) were supported in part by the National Science Foundation under Grant No. CTS-0227881. Access to the Hewlett-Packard V2500 computer, located at the California Institute of Technology, was provided by the Center for Advanced Computing Research.

[1] H. J. Lugt, *Vortex Flows in Nature and Technology* (Wiley, New York, 1983).
[2] P. R. Spalart, "Airplane trailing vortices," Annu. Rev. Fluid Mech. **30**, 107 (1998).
[3] L. Kelvin, "On the vibrations of a columnar vortex," Philos. Mag. **5**, 155 (1880).
[4] S. C. Crow, "Stability theory for a pair of trailing vortices," AIAA J. **8**, 2172 (1970).
[5] S. E. Widnall, D. B. Bliss, and C. Y. Tsai, "Instability of short waves on a vortex ring," J. Fluid Mech. **66**, 35 (1974).
[6] D. S. Pradeep and F. Hussain, "Core dynamics of a strained vortex: Instability and transition," J. Fluid Mech. **447**, 247 (2001).
[7] R. T. Pierrehumbert, "Universal short-wave instability of two-dimensional eddies in an inviscid fluid," Phys. Rev. Lett. **57**, 2157 (1986).
[8] B. J. Bayly, "Three-dimensional instability of elliptic flow," Phys. Rev. Lett. **57**, 2160 (1986).
[9] E. R. Hoffman and P. N. Joubert, "Turbulent line vortices," J. Fluid Mech. **16**, 395 (1963).
[10] S. P. Govindaraju and P. G. Saffman, "Flow in a turbulent trailing vortex," Phys. Fluids **14**, 2074 (1971).
[11] D. W. Moore and P. G. Saffman, "Axial flow in laminar trailing vortices," Proc. R. Soc. London, Ser. A **333**, 491 (1973).
[12] W. R. C. Phillips and J. A. H. Graham, "Reynolds-stress measurements in a turbulent trailing vortex," J. Fluid Mech. **147**, 353 (1984).
[13] S. Leibovich and K. Stewartson, "A sufficient condition for the instability of columnar vortices," J. Fluid Mech. **126**, 335 (1983).
[14] M. Sreedhar and S. Ragab, "Large eddy simulation of longitudinal stationary vortices," Phys. Fluids **6**, 2501 (1994).
[15] M. Sreedhar and S. Ragab, "Numerical simulation of vortices with axial velocity deficits," Phys. Fluids **7**, 549 (1995).
[16] L. Jacquin and C. Pantano, "On the persistence of trailing vortices," J. Fluid Mech. **471**, 159 (2002).
[17] A. B. Cain, J. H. Ferziger, and W. C. Reynolds, "Discrete orthogonal function expansions for non-uniform grids using the fast Fourier trans-

form," J. Comput. Phys. **56**, 272 (1984).
[18]G. E. Karniadakis, M. Israeli, and S. A. Orszag, "High-order splitting methods for the incompressible Navier-Stokes equations," J. Comput. Phys. **97**, 414 (1991).
[19]M. Frigo and S. G. Johnson, *IEEE International Conference on Acoustics, Speech, and Signal Processing (ICASSP) 1998*, Vol. 3, pp. 1381-1384.
[20]J. D. Buntine and D. I. Pullin, "Merger and cancellation of strained vortices," J. Fluid Mech. **205**, 263 (1989).
[21]R. Mallier and S. A. Maslowe, "A row of counter-rotating vortices," Phys. Fluids A **5**, 1074 (1993).
[22]S. Julien, J.-M. Chomaz, and J.-C. Lasheras, "Three-dimensional stability of periodic arrays of counter-rotating vortices," Phys. Fluids **14**, 732 (2002).
[23]J. T. Stuart, "On finite amplitude oscillations in laminar mixing layers," J. Fluid Mech. **29**, 417 (1967).
[24]D. W. Moore and P. G. Saffman, *Aircraft Wake Turbulence* (Plenum, New York, 1971), pp. 339–354.
[25]T. Leweke and C. H. K. Williamson, "Cooperative elliptic instability of a vortex pair," J. Fluid Mech. **360**, 85 (1998).
[26]P. E. Dimotakis, "The mixing transition in turbulent flows," J. Fluid Mech. **409**, 69 (2000).
[27]M. S. Chong, A. E. Perry, and B. J. Cantwell, "A general classification of three-dimensional flow fields," Phys. Fluids A **2**, 765 (1990).
[28]J. C. R. Hunt, A. A. Wray, and P. Moin, Center for Turbulence Research Report No. CTR-S88, 1988.
[29]J. Jeong and F. Hussain, "On the identification of a vortex," J. Fluid Mech. **285**, 69 (1995).
[30]S. Kida and H. Miura, "Identification and analysis of vortical structures," Eur. J. Mech. B/Fluids **17**, 471 (1998).
[31]P. G. Saffman, "A model of vortex reconnection," J. Fluid Mech. **212**, 395 (1990).
[32]B. Tao, J. Katz, and C. Meneveau, "Geometry and scale relationships in high reynolds number turbulence determined from three-dimensional holographic velocimetry," Phys. Fluids **12**, 941 (2000).
[33]R. M. Kerr, "Higher-order derivative correlations and the alignment of small-scale structures in isotropic numerical turbulence," J. Fluid Mech. **153**, 31 (1985).
[34]A. Misra and D. I. Pullin, "A vortex-based subgrid stress model for large-eddy simulation," Phys. Fluids **9**, 2443 (1997).
[35]T. S. Lundgren, "Strained spiral vortex model for turbulent fine structure," Phys. Fluids **25**, 2193 (1982).
[36]T. Veolkl, D. I. Pullin, and D. C. Chan, "A physical-space version of the stretched-vortex subgrid-stress model for large-eddy simulation," Phys. Fluids **12**, 1810 (2000).
[37]O. Metais and M. Lesieur, "Spectral large-eddy simulation of isotropic and stably stratified turbulence," J. Fluid Mech. **239**, 157 (1992).
[38]W. R. C. Phillips, "The turbulent trailing vortex during roll-up," J. Fluid Mech. **105**, 451 (1981).
[39]J. H. Konrad, "An experimental investigation of mixing in two-dimensional turbulent shear flows with applications to diffusion-limited chemical reactions," Ph.D. thesis, Caltech, 1977.
[40]R. Breidenthal, "Structure in turbulent mixing layers and wakes using a chemical reaction," J. Fluid Mech. **109**, 1 (1981).
[41]K. R. Sreenivasan, "An update on the energy dissipation rate in isotropic turbulence," Phys. Fluids **10**, 528 (1998).
[42]K. R. Sreenivasan, "On the scaling of the turbulent energy dissipation rate," Phys. Fluids **27**, 867 (1984).